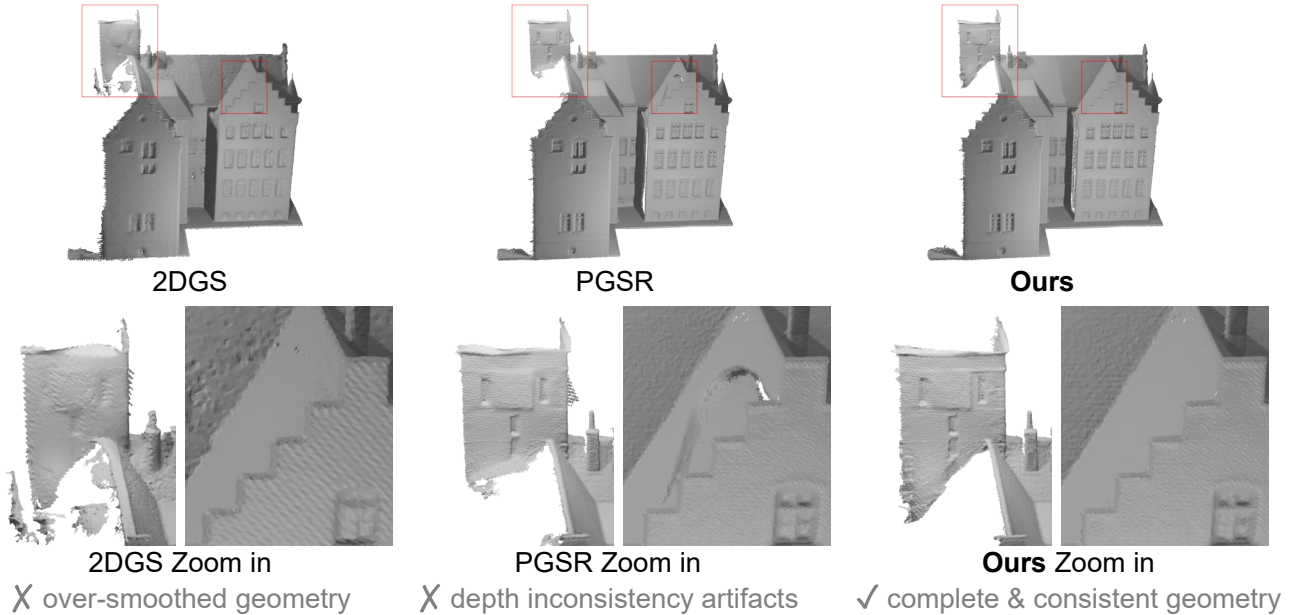


GVGS: Gaussian Visibility-Aware Multi-View Geometry for Accurate Surface Reconstruction

Mai Su¹, Qihan Yu¹, Zhongtao Wang¹, Yilong Li¹, Chengwei Pan², Yisong Chen¹, Guoping Wang^{1,*}, Fei Zhu^{1,*}

¹School of Computer Science, Peking University

²Institute of Artificial Intelligence, Beihang University



Depth/flow-based visibility is unreliable, while Gaussian-level visibility enables consistent geometry.

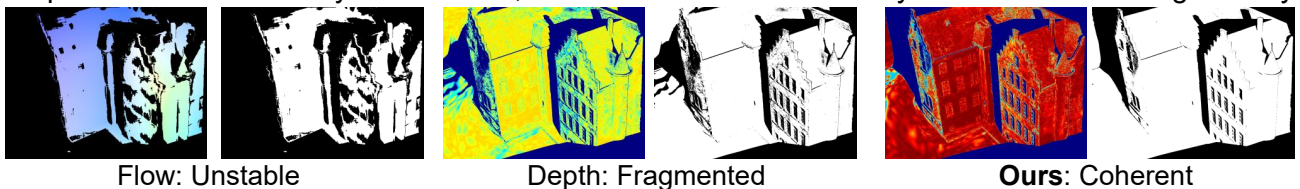


Figure 1: Modeling visibility is critical for accurate surface reconstruction. Existing methods suffer from unreliable visibility estimation: depth-based approaches produce fragmented supervision [3], while flow-based methods introduce noisy correspondence [24]. As shown in the top comparisons, these issues lead to over-smoothed geometry (2DGS [13]) and depth inconsistency artifacts (PGSR [3]). In contrast, our Gaussian-level visibility modeling aggregates cross-view contributions of shared Gaussians, producing a coherent visibility signal that enables consistent geometry reconstruction. For visualization, warmer colors indicate stronger visibility intensity.

Abstract

3D Gaussian Splatting (3DGS) enables efficient rendering, yet accurate surface reconstruction remains challenging due to unreliable geometric supervision. Existing approaches predominantly rely on depth-based reprojection to infer visibility and enforce multi-view consistency, leading to a fundamental circular dependency: visibility estimation requires accurate depth, while depth supervision itself is conditioned on visibil-

ity. In this work, we revisit multi-view geometric supervision from the perspective of visibility modeling. Instead of inferring visibility from pixel-wise depth consistency, we explicitly model visibility at the level of Gaussian primitives. We introduce a Gaussian visibility-aware multi-view geometric consistency (GVMV) formulation, which aggregates cross-view visibility of shared Gaussians to construct reliable supervision over co-visible regions. To further incorporate monocular priors, we propose a progressive quadtree-calibrated depth

alignment (QDC) strategy that performs block-wise affine calibration under visibility-aware guidance, effectively mitigating scale ambiguity while preserving local geometric structures. Extensive experiments on DTU and Tanks and Temples demonstrate that our method consistently improves reconstruction accuracy over prior Gaussian-based approaches. Our code is fully open-sourced and available at an anonymous repository: <https://github.com/GVGScode/GVGS>.

1 Introduction

3D Gaussian Splatting (3DGS) [16] has recently emerged as a powerful and efficient representation for novel view synthesis, offering high-quality rendering with significantly reduced training and rendering cost compared to neural implicit radiance fields [1, 23, 25]. By directly optimizing geometric and appearance parameters with rasterization-based rendering, 3DGS has quickly become a strong foundation for real-time and large-scale scene representation. However, despite its success in appearance modeling, accurately recovering surface geometry from 3DGS remains challenging, as the representation is inherently optimized for rendering rather than precise geometric reconstruction.

A core challenge lies in the reliability of geometric supervision under multi-view settings. Under purely photometric supervision, the volumetric and unstructured nature of Gaussian primitives allows them to drift away from true surfaces while still explaining image observations, leading to geometric ambiguity, thickness artifacts, and degraded multi-view consistency [32]. To address this issue, recent works introduce geometry-aware regularization into the 3DGS framework, such as depth and normal priors or local smoothness constraints [4, 30]. Meanwhile, other approaches reformulate Gaussian primitives as surface-aligned elements, including planar-based representations [3], surfel-based or 2D Gaussian formulations [12, 13, 35], and hybrid methods combining Gaussian splatting with implicit geometry fields [14, 19, 37]. These advances highlight the importance of incorporating geometric structure into Gaussian representations for accurate surface reconstruction.

Despite these efforts, existing methods rely heavily on depth-based supervision, assuming that visibility can be inferred from depth reprojection. This leads to a fundamental circular dependency: visibility estimation depends on accurate depth, while depth supervision itself is conditioned on visibility. Consequently, when depth becomes unreliable—e.g., under occlusion, wide baselines, or weak textures—both visibility estimation and geometric supervision degrade, resulting in unstable optimization and inferior reconstruction quality.

To alleviate this issue, monocular depth and normal priors are often introduced to guide Gaussian optimization [21, 30]. However, these priors suffer from scale ambiguity and local inconsistency, and without proper alignment may introduce artifacts or oversmooth fine structures. As a result, simply combining multi-view depth consistency with monocular priors does not fully resolve the underlying limitation.

In this paper, we revisit multi-view geometric supervision

from the perspective of visibility modeling. We argue that the fundamental limitation of existing methods does not lie solely in inaccurate depth estimation, but in the underlying assumption that visibility can be reliably inferred from depth reprojection. This assumption introduces an inherent circular dependency: visibility estimation requires accurate depth, while geometric supervision itself is conditioned on visibility. As a result, once depth becomes unreliable, both visibility estimation and geometric constraints degrade simultaneously.

Based on this insight, we introduce a Gaussian visibility-aware multi-view geometric consistency (GVMV) formulation. Our method estimates per-Gaussian visibility in a neighboring view by aggregating its rendering contributions, and uses this information to construct a visibility-aware supervision signal in the reference view. This formulation allows geometric consistency to be enforced over a broader set of co-visible regions, rather than being restricted to areas where depth reprojection is already reliable.

To further incorporate monocular priors, we propose a progressive quadtree-calibrated depth alignment strategy, which aligns monocular depth with Gaussian-rendered geometry under visibility-aware guidance. By performing coarse-to-fine, block-wise affine calibration, our method mitigates scale ambiguity while preserving fine-grained local structures, enabling monocular depth to serve as an effective geometric prior.

In summary, our contributions are threefold:

- **Rethinking visibility modeling in multi-view supervision.** We identify a fundamental circular dependency in existing depth-based formulations, which leads to unreliable geometric supervision.
- **Gaussian visibility-aware multi-view geometry.** We propose a Gaussian-level visibility modeling framework that explicitly captures cross-view co-visibility and enables robust geometric consistency beyond depth-reliable regions.
- **Visibility-guided monocular depth alignment.** We introduce a quadtree-calibrated depth alignment strategy that integrates monocular priors under visibility-aware guidance, improving both global consistency and local geometric fidelity.

2 Related Works

Novel View Synthesis Neural radiance field (NeRF) based methods model scenes as continuous volumetric fields optimized via differentiable rendering and are widely used for novel view synthesis [11, 23], but incur high computational cost due to dense ray marching and neural networks [1]. As an efficient alternative, 3D Gaussian Splatting (3DGS) represents scenes with anisotropic Gaussian primitives and renders via rasterization [16], enabling fast optimization and real-time or near-real-time performance. Building on this representation, subsequent works have further improved rendering quality and efficiency [7, 38], and extended it to large-scale [17, 29], dynamic [6, 22], and sparse-view scenarios [5, 40].

Gaussian Splatting for Surface Reconstruction To explicitly recover surface geometry from Gaussian splatting, prior work reformulates Gaussian primitives into surface-oriented representations. SuGaR [12] introduces a surface-alignment regularizer that encourages Gaussians to form locally surface-tangent configurations, and derives an approximate distance function for efficient mesh extraction via Poisson reconstruction [15]. Planar-based formulations reinterpret anisotropic Gaussians as locally planar primitives, enabling unbiased depth and normal rendering and facilitating geometry-aware constraints [3]. More generally, subsequent works constrain Gaussians to planar or disk-like configurations to better adhere to underlying surfaces [13, 35, 41]. In parallel, recent approaches address transparent surface reconstruction by learning transparency attributes to handle view-dependent appearance and geometric ambiguities [18].

Another line of work combines Gaussian splatting with implicit geometry fields to leverage the complementary strengths of explicit and continuous representations. Methods such as GSDF and GaussianUDF jointly optimize Gaussian primitives with signed or unsigned distance functions to guide surface reconstruction while retaining efficient rendering [19, 37]. Geometry Field Splatting further unifies this paradigm by representing geometry fields with Gaussian surfels and deriving an efficient differentiable rendering formulation, establishing a more principled connection between Gaussian splatting and implicit geometry [14]. GOF models surfaces via a compact continuous opacity field over Gaussian primitives, enabling efficient and memory-compact reconstruction in unbounded scenes without explicit distance fields or dense volumetric sampling [39].

Geometric Constraints for Gaussian-based Surface Reconstruction Beyond representation-level designs, recent work improves Gaussian-based surface reconstruction by incorporating geometric constraints during optimization. 2DGS [13] introduces a normal consistency constraint to explicitly model per-Gaussian surface normals and enforce alignment with depth-derived normals, stabilizing disk-like primitives. DN-Splatter [30] aligns Gaussian orientations with monocular normal priors and further imposes local smoothness to enforce consistency of depth, normal, and scale among neighboring Gaussians. PGSR [3] proposes a multi-view geometric consistency loss that jointly enforces depth and photometric consistency across views by constraining shared planar Gaussian structures, drawing inspiration from classical multi-view stereo formulations [2]. These methods highlight the importance of geometric regularization for accurate surface reconstruction, but typically assume reliable depth estimation or consistent cross-view scale.

Despite their effectiveness, existing multi-view constraints still rely on accurate Gaussian depth and are sensitive to depth bias in challenging regions, while monocular supervision does not explicitly address cross-view scale ambiguity. Our method addresses these limitations by explicitly modeling cross-view visibility at the Gaussian level and introducing a quadtree-calibrated monocular depth constraint, enabling more robust multi-view supervision and reliable single-view depth guidance

under imperfect depth priors.

3 Method

Given a set of calibrated multi-view RGB images, we reconstruct scene geometry using Gaussian splatting by jointly leveraging multi-view geometric cues and monocular depth priors. An overview of the proposed framework is illustrated in Fig. 2.

Our method consists of two key components: (1) Gaussian visibility-aware multi-view geometric consistency (GVMV), which models cross-view visibility at the Gaussian level to provide reliable geometric supervision; and (2) a quadtree-calibrated depth constraint (QDC), which refines monocular depth to offer coarse structural guidance during training. We first review the formulation of 3D Gaussian Splatting, followed by our two components, GVMV and QDC, and finally present the overall training objective.

3.1 Preliminary: 3D Gaussian Splatting

3D Gaussian Splatting (3DGS) [16] represents a scene as a collection of learnable 3D Gaussian primitives distributed in space. Each Gaussian is parameterized by a center $\mu \in \mathbb{R}^3$ and an anisotropic covariance matrix $\Sigma \in \mathbb{R}^{3 \times 3}$, which together define its spatial extent and density contribution.

$$G(\mathbf{x}) = \exp\left(-\frac{1}{2}(\mathbf{x} - \mu)^\top \Sigma^{-1}(\mathbf{x} - \mu)\right), \quad (1)$$

where $\mathbf{x} \in \mathbb{R}^3$ denotes a 3D query location. In addition to its geometric parameters, each Gaussian is associated with an opacity value $\alpha \in [0, 1]$ and appearance features that encode view-dependent color.

During rendering, the 3D Gaussian primitives are transformed into the image plane via the camera projection, giving rise to corresponding 2D Gaussian footprints:

$$G'(\mathbf{x}') = \exp\left(-\frac{1}{2}(\mathbf{x}' - \mu')^\top \Sigma'^{-1}(\mathbf{x}' - \mu')\right), \quad (2)$$

where $\mathbf{x}' \in \mathbb{R}^2$ denotes a pixel location. The final pixel color is obtained by compositing the projected Gaussians in a depth-sorted order via alpha blending:

$$C(\mathbf{x}') = \sum_i T_i \alpha_i(x) G'_i(\mathbf{x}') c_i, \quad T_i = \prod_{j=1}^{i-1} (1 - \alpha_j(x) G'_j(\mathbf{x}')), \quad (3)$$

where c_i denotes the color of the i -th Gaussian. As the entire splatting and compositing process is fully differentiable, all Gaussian parameters can be optimized end-to-end by minimizing photometric reconstruction errors.

3.2 Gaussian Visibility-Aware Multi-View Geometric Consistency

Previous Gaussian-based surface reconstruction methods enforce multi-view geometric consistency through pixel-wise depth constraints. Specifically, these approaches reproject

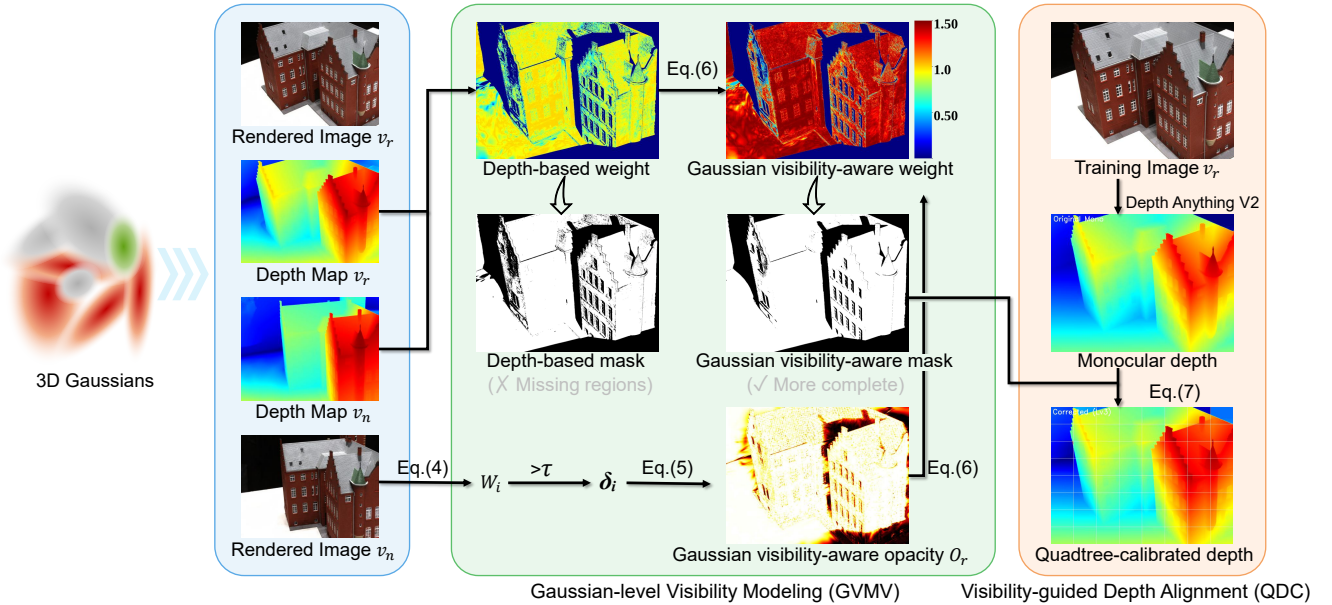


Figure 2: Overview of GVGS. Given 3D Gaussians, we render RGB images and depth maps from a reference view v_r and a neighboring view v_n . Unlike conventional depth-based supervision that infers visibility implicitly and yields incomplete masks under occlusion, we explicitly model cross-view visibility at the Gaussian level. We compute per-Gaussian visibility weights W_i in v_n (Eq. (4)) and obtain binary indicators δ_i , which are projected back to v_r to construct a visibility-aware opacity O_r (Eq. (5)). This produces a more complete supervision mask over co-visible regions and enables the Gaussian visibility-aware geometric consistency loss $L_{gvmvgeom}$ (Eq. (6)). In parallel, we introduce a visibility-guided quadtree-calibrated depth alignment (QDC), where monocular depth (Depth-Anything V2) is progressively aligned to Gaussian-rendered depth to define L_{qdc} (Eq. (7)). Both depth-based and visibility-aware weights share the same color bar for visualization.

Gaussian-derived depth maps into neighboring views and penalize discrepancies; we refer readers to PGSR [3] for representative implementations. However, such formulations rely on the assumption that depth estimates are sufficiently accurate to infer visibility, which often breaks down under occlusion, large baselines, or geometric inconsistencies, as illustrated by the “Depth-based” subfigure in Fig. 1, where reprojection constraints fail on the left building facade.

More fundamentally, existing methods implicitly assume that visibility can be reliably inferred from depth reprojection. However, this introduces a circular dependency: visibility estimation depends on accurate depth, while geometric supervision itself is conditioned on visibility. As a result, once depth estimates become unreliable, both visibility estimation and geometric supervision degrade simultaneously.

To address this issue, we introduce the following principle: **multi-view geometric consistency should be enforced over all pixels that are co-visible across neighboring views**, rather than being restricted to regions where depth reprojection is already consistent. Unlike prior methods that infer visibility implicitly from depth or patch consistency [8, 28], **we explicitly model visibility at the level of Gaussian primitives**.

We therefore introduce a **Gaussian-based visibility estimation** to explicitly capture cross-view co-visibility, and further develop a **Gaussian visibility-aware multi-view geometric consistency** formulation to enforce geometric supervision over co-visible regions. An overview is shown in Fig. 2.

Gaussian-based Visibility Estimation. Given a reference view v_r and a neighboring view v_n , our goal is to determine which Gaussian primitives are visible in v_n , and therefore should contribute to cross-view supervision.

To this end, we explicitly estimate the rendering contribution of each Gaussian primitive during the differentiable rasterization of the neighboring view v_n . We define the visibility weight of each Gaussian based on its rendering influence on the image, resulting in $W_i \in \mathbb{R}^+$:

$$W_i = \sum_{\mathbf{x} \in \Omega_n} \alpha_i(\mathbf{x}) \cdot T_i(\mathbf{x}), \quad (4)$$

where $\alpha_i(\mathbf{x})$ denotes the opacity contribution of g_i at pixel \mathbf{x} , and $T_i(\mathbf{x})$ is the accumulated transmittance under standard alpha compositing (Eq. (3)).

Intuitively, W_i measures how much Gaussian g_i contributes to the rendering of view v_n . We then define a binary visibility indicator $\delta_i = \mathbb{I}(W_i > \tau)$, where τ is a small threshold to suppress negligible contributions.

Visibility Projection to the Reference View. We next transfer the estimated visibility back to the reference view v_r . Specifically, we construct a selectively accumulated opacity map:

$$O_r(\mathbf{x}) = \sum_i \delta_i \alpha_i(\mathbf{x}) \prod_{j < i} (1 - \alpha_j(\mathbf{x})), \quad (5)$$

where δ_i acts as a visibility gate that activates only those Gaussians that are visible in v_n .

As a result, $O_r(\mathbf{x})$ aggregates the contributions of Gaussians that are co-visible across the two views, while preserving the standard depth-ordered alpha compositing structure. Importantly, $O_r(\mathbf{x})$ is not a simple opacity accumulation, but a Gaussian-level visibility-aware weighting term that encodes cross-view co-visibility. This design enables reliable supervision even in regions where depth-based reprojection fails, as illustrated in Fig. 1, where facade regions with large depth discrepancies are still correctly constrained.

Gaussian Visibility-Aware Geometric Consistency. We build upon the multi-view geometric consistency loss L_{mvgeom} introduced in PGSR [3]. Each reference pixel \mathbf{x} is associated with a forward-backward reprojection error $\phi(\mathbf{x})$, which is mapped to a confidence weight via a monotonic function such as $\exp(-\phi(\mathbf{x}))$. Pixels with large reprojection errors (e.g., $\phi(\mathbf{x}) > 1$) are typically excluded from supervision.

We extend this formulation by incorporating Gaussian-level visibility information through $O_r(\mathbf{x})$. This allows geometric supervision to be applied over a broader set of co-visible regions, instead of being limited to areas where depth reprojection is already reliable. As shown in Fig. 2, regions that were previously unsupervised (e.g., facade areas) become effectively constrained.

The resulting Gaussian visibility-aware multi-view geometric consistency loss is defined as

$$L_{gvmvgeom} = \frac{1}{|\mathcal{V}|} \sum_{\mathbf{x} \in \mathcal{V}} (\exp(-\phi(\mathbf{x})) + \lambda O_r(\mathbf{x})) \phi(\mathbf{x}), \quad (6)$$

where \mathcal{V} is constructed as the union of: (i) pixels satisfying conventional depth-based consistency, and (ii) pixels identified as co-visible by our Gaussian visibility-aware opacity. The parameter λ controls the relative contribution of the visibility term.

3.3 Quadtree-calibrated Monocular Depth Constraint

Recent advances in large-scale vision models have enabled highly detailed monocular depth prediction from a single image [33, 34]. However, when integrated into multi-view reconstruction pipelines, monocular depth exhibits two inherent limitations: *scale ambiguity* and *view-dependent bias*. These issues often lead to misalignment between monocular depth and the geometry represented by Gaussians, resulting in biased gradients and unstable optimization.

Existing approaches typically mitigate this problem by applying a global scale-and-shift calibration using sparse COLMAP SfM points, or by restricting supervision to pixels that satisfy multi-view reprojection consistency [9, 17]. However, such strategies fail to address spatially varying depth bias, and cannot ensure consistent alignment between monocular depth and Gaussian-rendered geometry across complex scenes.

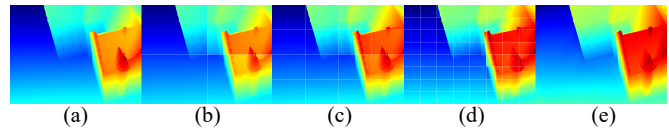


Figure 3: Progressive quadtree depth calibration. (a) Raw monocular depth and (e) Gaussian-rendered depth show clear bias. (b–d) Coarse-to-fine block-wise affine calibration (Lv1–Lv3) progressively aligns monocular and rendered depth.

To address this limitation, we introduce a **quadtree-calibrated depth alignment** strategy. Instead of applying a single global calibration, we progressively align monocular depth with Gaussian-rendered depth at multiple spatial scales, under the guidance of reliable geometric regions identified by our visibility-aware formulation.

Coarse-to-fine Quadtree Alignment. During training, we adopt a coarse-to-fine quadtree schedule. At iteration t , we select a quadtree level $L(t) \in \{0, \dots, L_{\max}\}$ and partition the image into $2^{L(t)} \times 2^{L(t)}$ blocks. As training proceeds, $L(t)$ is gradually increased, allowing depth alignment to transition from global coarse calibration to fine-grained local refinement.

For each quadtree block \mathcal{B}_k , we align the monocular depth $D_m(\mathbf{x})$ to the Gaussian-rendered depth $D_g(\mathbf{x})$ using a block-wise affine model [27]:

$$\begin{aligned} D'_m(\mathbf{x}) &= a_k D_m(\mathbf{x}) + b_k, & \mathbf{x} \in \mathcal{B}_k \cap \mathcal{V}, \\ a_k &= \frac{\sigma_{\mathbf{y} \in \mathcal{B}_k}(D_g(\mathbf{y}))}{\sigma_{\mathbf{y} \in \mathcal{B}_k}(D_m(\mathbf{y}))}, \\ b_k &= \mu_{\mathbf{y} \in \mathcal{B}_k}(D_g(\mathbf{y}) - a_k D_m(\mathbf{y})), \end{aligned} \quad (7)$$

where (a_k, b_k) denote the affine calibration parameters associated with block \mathcal{B}_k . Here, $\mu(\cdot)$ and $\sigma(\cdot)$ denote robust estimators of location and scale, implemented as the median and the mean absolute deviation about the median.

Intuitively, this formulation aligns monocular depth to Gaussian-rendered geometry in a locally adaptive manner. Coarse quadtree levels correct global scale mismatch, while finer levels capture spatially varying bias. Moreover, calibration is restricted to pixels within \mathcal{V} , i.e., regions that are either validated by multi-view reprojection or identified as co-visible through Gaussian visibility (Eq. (6)), ensuring that alignment is guided by reliable geometric regions.

The affine parameters are recomputed only when the quadtree level $L(t)$ increases and reused across subsequent iterations, resulting in negligible computational overhead. As illustrated in Fig. 3, this progressive strategy yields increasingly accurate alignment, particularly in regions with large initial depth bias (e.g., rooftop areas).

Quadtree-calibrated Monocular Depth Constraint. After alignment, the calibrated monocular depth $D'_m(\mathbf{x})$ is supervised against the Gaussian-rendered depth $D_g(\mathbf{x})$ using an ℓ_1 loss:

$$L_{qdc} = \sum_{\mathbf{x} \in \mathcal{V}} \|D'_m(\mathbf{x}) - D_g(\mathbf{x})\|_1, \quad (8)$$

Table 1: **Chamfer Distance on DTU (lower is better)**. For each scan, the best, second, and third results are highlighted with red, orange, and yellow backgrounds, respectively.

CD (mm)↓	24	37	40	55	63	65	69	83	97	105	106	110	114	118	122	Mean	Time
NeuS [31]	1.00	1.37	0.93	0.43	1.10	0.65	0.57	1.48	1.09	0.83	0.52	1.20	0.35	0.49	0.54	0.84	>12h
VolSDF [36]	1.14	1.26	0.81	0.49	1.25	0.70	0.72	1.29	1.18	0.70	0.66	1.08	0.42	0.61	0.55	0.86	>12h
Neuralangelo [20]	0.37	0.72	0.35	0.35	0.87	0.54	0.53	1.29	0.97	0.73	0.47	0.74	0.32	0.41	0.43	0.61	>128h
3DGS [16]	2.14	1.53	2.08	1.68	3.49	2.21	1.43	2.07	2.22	1.75	1.79	2.55	1.53	1.52	1.50	1.96	11.2min
SuGaR [12]	1.47	1.33	1.13	0.61	2.25	1.71	1.15	1.63	1.62	1.07	0.79	2.45	0.98	0.88	0.79	1.33	1h
2DGS [13]	0.48	0.91	0.39	0.39	1.01	0.83	0.81	1.36	1.27	0.76	0.70	1.40	0.40	0.76	0.52	0.80	19.2min
GOF [39]	0.50	0.82	0.37	0.37	1.12	0.74	0.73	1.18	1.29	0.68	0.77	0.90	0.42	0.66	0.49	0.74	1h
QGS [41]	0.42	0.65	0.36	0.37	0.85	0.65	0.50	1.14	0.97	0.61	0.48	0.67	0.34	0.41	0.37	0.59	48min
PGSR [3]	0.39	0.54	0.39	0.36	0.78	0.57	0.49	1.07	0.64	0.59	0.47	0.54	0.30	0.37	0.34	0.52	40min
Ours	0.32	0.53	0.33	0.33	0.79	0.52	0.47	1.05	0.63	0.58	0.37	0.53	0.30	0.35	0.32	0.49	43min

Table 2: **Quantitative F1-score comparison on the TNT dataset** (higher is better). The best/second/third results are highlighted in red, orange, and yellow.

F1-Score↑	N-angelo	2DGS	GOF	PGSR	QGS	Ours(30k)	Ours(60k)
Barn	0.70	0.41	0.51	0.56	0.55	0.54	0.58
Caterpillar	0.36	0.24	0.41	0.41	0.40	0.44	0.47
Courthouse	0.28	0.16	0.28	0.26	0.28	0.22	0.24
Ignatius	0.89	0.52	0.68	0.79	0.81	0.80	0.81
Meetingroom	0.32	0.17	0.28	0.34	0.31	0.36	0.39
Truck	0.48	0.45	0.58	0.65	0.64	0.68	0.68
Mean	0.50	0.33	0.46	0.50	0.50	0.51	0.53
Time	>127h	34min	114min	66min	75min	69min	117min

where \mathcal{V} denotes the trusted region defined in Eq. (6).

This monocular depth is only used in early training to provide coarse geometric guidance, rather than serving as final supervision. By restricting supervision to visibility-aware regions and performing coarse-to-fine local alignment, our formulation enables monocular depth to serve as a stable and accurate geometric prior. This improves both global consistency and local structural detail, while remaining robust to noisy or biased depth predictions.

3.4 Training Objective

The overall training objective is formulated as a weighted sum of multiple loss terms:

$$L = L_{rgb} + \lambda_1 L_s + \lambda_2 L_{mvr gb} + \lambda_3 L_{gvmvgeom} + \lambda_4 L_{qdc}, \quad (9)$$

where λ_1 – λ_4 are scalar weights that balance the contributions of the individual loss terms.

Here, L_{rgb} denotes the standard photometric reconstruction loss in 3D Gaussian Splatting, which combines ℓ_1 and SSIM terms. Following PGSR, we directly adopt single-view depth and normal supervision via L_s , together with a multi-view photometric consistency loss $L_{mvr gb}$ [3]. Building upon these components, we introduce our proposed Gaussian visibility-aware multi-view geometric consistency loss $L_{gvmvgeom}$ and the quadtree-calibrated monocular depth loss L_{qdc} , which together enable robust geometric supervision and adaptive calibration of monocular depth priors throughout training.

4 Experiments

4.1 Datasets

We evaluate our method on two standard multi-view surface reconstruction benchmarks: **DTU** and **Tanks and Temples (TNT)**. DTU consists of calibrated indoor scenes with high-quality structured-light ground-truth geometry. Following prior work [3], we report results on the standard 15 scans using symmetric Chamfer Distance, without explicit alignment between reconstructed geometry and ground-truth point clouds. We use the DTU data preprocessed by 2DGS [13].

The Tanks and Temples (TNT) benchmark contains large-scale indoor and outdoor scenes. We evaluate on the *Intermediate* set of six scenes (Barn, Caterpillar, Courthouse, Ignatius, Meetingroom, and Truck), reporting per-scene F-score (F1). We adopt the TNT data from GOF [39] and follow the evaluation protocol of QGS [41].

4.2 Implementation Details

Our implementation builds upon PGSR [3], inheriting most default hyperparameters, and uses monocular depth priors from Depth Anything v2 [34], which are further calibrated via the proposed quadtree-calibrated depth constraint. The influence computation follows EAGLES [10]. For DTU, each scene is trained for 30k iterations, during which the quadtree split level $L(t)$ is progressively increased at 10k, 15k, and 20k iterations. The quadtree-calibrated monocular depth loss L_{qdc} is activated from 7k to 25k iterations to ensure stable optimization. Negligible Gaussian contributions are filtered using a threshold $\tau = 0.0001$, with Gaussians below this threshold considered non-visible in the neighboring view. We set the visibility weighting coefficient λ in Eq. (6) to 0.5. For Tanks and Temples (TNT), each scene is trained for 60k iterations with corresponding hyperparameters adjusted accordingly. Meshes are extracted via TSDF fusion [26]. All experiments are conducted on an Ubuntu server equipped with four NVIDIA A6000 GPUs (48 GB memory each). Additional implementation details are provided in our code.

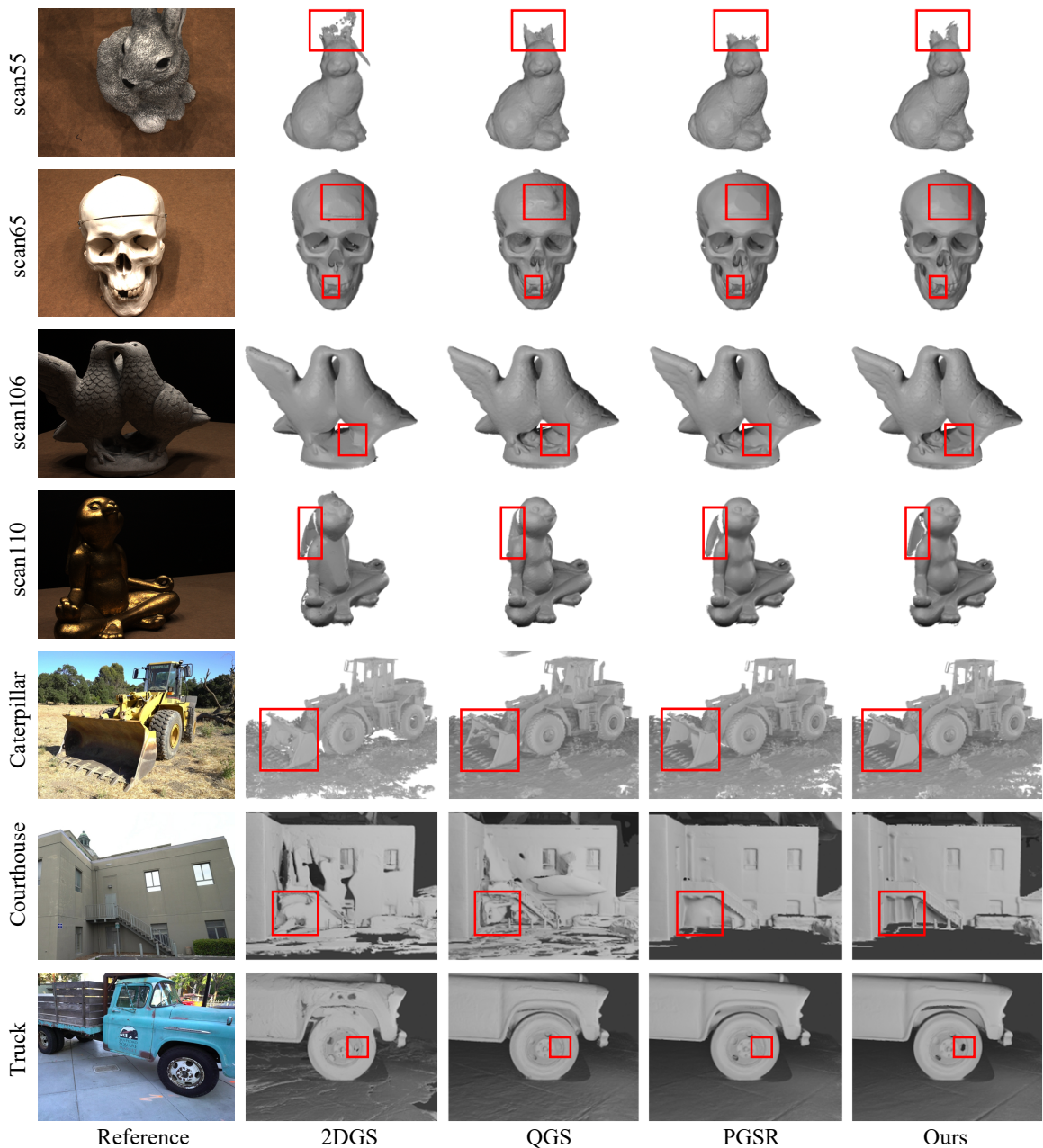


Figure 4: Qualitative Comparison of Reconstructed Geometry with Related Works on DTU and Tanks and Temples. Red boxes highlight regions with noticeable geometric differences.

4.3 Comparison

For geometry evaluation, we follow the standard protocol of recent Gaussian-based methods and conduct all experiments on DTU and TNT at *half resolution*. Chamfer Distance and F-score are reported as the primary geometry metrics. We quantitatively compare our method with implicit surface methods [20, 31, 36] and Gaussian-based surface reconstruction approaches [3, 12, 13, 16, 39, 41]. We reproduce the results of PGSR [3] and QGS [41] using their official implementations, and adopt the remaining baselines from QGS [41].

For DTU dataset, as shown in Table 1, our method achieves the best Chamfer Distance on **14 out of the 15** evaluated scans.

In terms of overall accuracy, our approach attains a mean Chamfer Distance of **0.49 mm (0.4933 mm before rounding)**, improving upon the best prior result by approximately **5%**. As illustrated in Fig. 4, our method produces more complete rabbit ears, smoother skull forehead surfaces, more faithful reconstruction of dental cavities, and a clearer separation between the bird’s feet and the supporting base. We attribute these improvements to the stronger geometric constraints introduced by our method, which provide more reliable supervision in regions with uneven illumination and sparse viewpoints. Despite additional geometric supervision, our method incurs only minimal overhead and maintains comparable training efficiency to existing

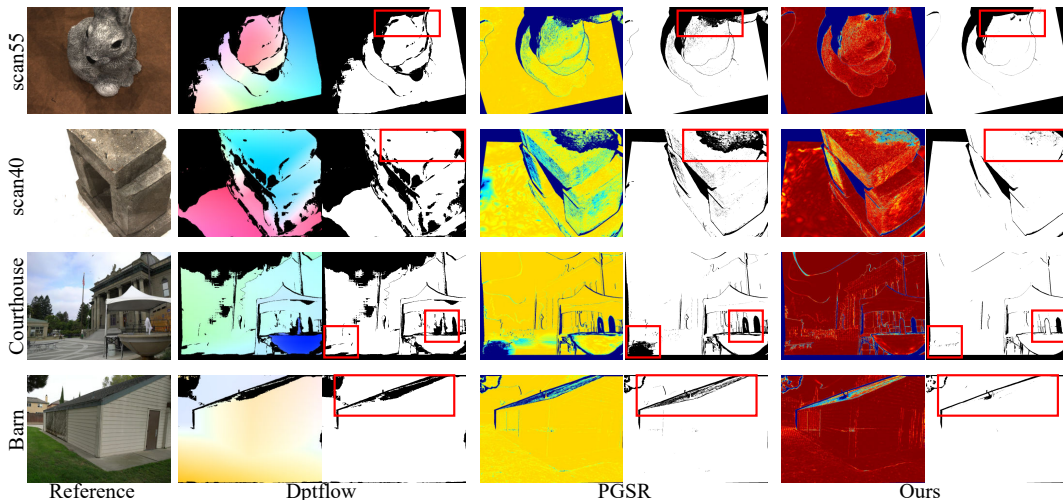


Figure 5: Qualitative comparison of visibility masks across different methods.

Gaussian-based approaches.

For the **Tanks and Temples** benchmark, Table 2 reports quantitative F1-score results. Our method achieves the highest average F1-score of **0.53 (0.5302 before rounding)**, outperforming all compared approaches. Specifically, it attains the best performance on **3 of the 6** scenes and ranks second on two, indicating strong and consistent reconstruction quality. As shown in Fig. 4, only our method reconstructs the *Caterpillar* bucket without holes and avoids depth artifacts on the left side. Moreover, it is the only method that correctly recovers the pillar beneath the staircase and the associated wall details in the *Courthouse* scene, and also achieves the most faithful reconstruction of the hollow wheel hub structures in the *Truck* scene.

Visibility Comparison. Although no multi-view dataset provides ground-truth visibility masks, we qualitatively compare the predicted visibility across methods. We compare visibility masks produced by a flow-based method, DPFlow [24], and a depth-based method, PGSR [3], as shown in Fig. 5. Flow-based visibility is often noisy and unstable due to unreliable motion estimation, while depth-based visibility is sensitive to depth inaccuracies and leads to fragmented masks. In contrast, our Gaussian-level visibility modeling produces cleaner and more coherent masks, providing more reliable supervision over co-visible regions.

Table 3: Ablation study on DTU and TNT.

Setting	CD (DTU) ↓	F1 (TNT) ↑
Full	0.493	0.530
w/o QDC	0.505	0.520
w/o QDC + MonoD	0.512	0.513
w/o QDC + MonoD + GVMV	0.519	0.503
w/o GVMV	0.511	0.512

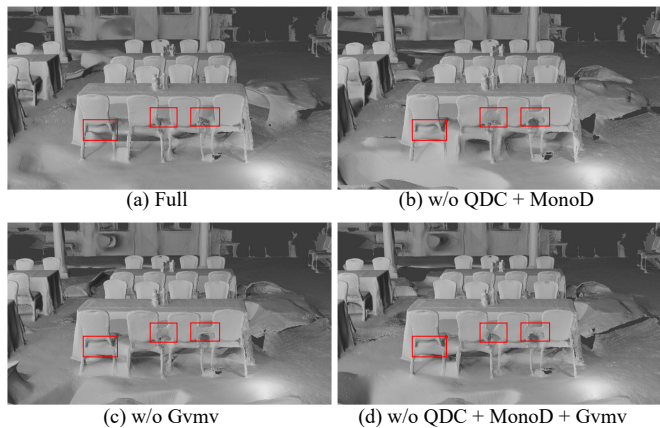


Figure 6: Qualitative ablation of the proposed components on *Meetingroom*. Red boxes highlight failure cases.

4.4 Ablation Studies

We evaluate the contribution of each component via ablation. Starting from the full model (**Full**), we progressively remove: (1) the quadtree-calibrated depth constraint (**w/o QDC**), where Gaussian depth is directly supervised by monocular depth [34]; (2) monocular depth supervision (**w/o QDC + MonoD**); (3) the Gaussian visibility-aware multi-view geometric consistency (**w/o QDC + MonoD + GVMV**); and (4) only GVMV (**w/o GVMV**) to isolate its effect.

As shown in Table 3, ablation results on DTU and Tanks and Temples (TNT) show that removing any component consistently degrades reconstruction performance in terms of Chamfer Distance and F1. We further provide qualitative comparisons on the *Meetingroom* scene from TNT in Fig. 6, where the progressive degradation in chair structures highlights the complementary role of each component. Together, these results provide consistent quantitative and visual evidence of our design effectiveness.

We also evaluate the sensitivity of the visibility threshold τ .

Table 4: Ablation on the visibility threshold τ . Performance is stable for small τ , with the best result at $\tau = 1e-4$.

τ	1e-5	1e-4	1e-3	1e-2	1e-1	1	10	Soft
CD↓ (DTU)	0.493	0.493	0.497	0.497	0.497	0.499	0.503	0.497
F1↑ (TNT)	0.529	0.530	0.529	0.529	0.529	0.526	0.524	0.529

As shown in Table 4, the performance remains stable across a wide range of small τ values, indicating that our method is not sensitive to the exact threshold choice. When τ becomes large, performance gradually degrades due to overly strict visibility filtering. We also evaluate a soft visibility weighting formulation, which achieves comparable results but does not show clear advantages.

5 Conclusion

We present a Gaussian visibility-aware multi-view geometric consistency formulation together with a quadtree-calibrated monocular depth constraint, which provide richer geometric supervision and lead to consistent improvements in surface reconstruction quality.

Our method also produces high-quality multi-view visibility masks as a byproduct, which can benefit a wide range of tasks, including multi-view semantic segmentation, scene understanding, and geometry-aware rendering and editing. We hope this capability inspires future exploration of Gaussian-based visibility reasoning as a general geometric prior for multi-view vision and graphics.

A current limitation of our method is the lack of dedicated modeling for highly specular or transparent surfaces, which we leave for future work.

References

- [1] Jonathan T Barron, Ben Mildenhall, Matthew Tancik, Peter Hedman, Ricardo Martin-Brualla, and Pratul P Srinivasan. Mip-nerf: A multiscale representation for anti-aliasing neural radiance fields. In *Proceedings of the IEEE/CVF international conference on computer vision*, pages 5855–5864, 2021.
- [2] Neill DF Campbell, George Vogiatzis, Carlos Hernández, and Roberto Cipolla. Using multiple hypotheses to improve depth-maps for multi-view stereo. In *European conference on computer vision*, pages 766–779. Springer, 2008.
- [3] Danpeng Chen, Hai Li, Weicai Ye, Yifan Wang, Weijian Xie, Shangjin Zhai, Nan Wang, Haomin Liu, Hujun Bao, and Guofeng Zhang. Pgsr: Planar-based gaussian splatting for efficient and high-fidelity surface reconstruction. *IEEE Transactions on Visualization and Computer Graphics*, 2024.
- [4] Hanlin Chen, Fangyin Wei, Chen Li, Tianxin Huang, Yunsong Wang, and Gim Hee Lee. Vcr-gaus: View consistent depth-normal regularizer for gaussian surface reconstruction. *Advances in Neural Information Processing Systems*, 37:139725–139750, 2024.
- [5] Yuedong Chen, Haofei Xu, Chuanxia Zheng, Bohan Zhuang, Marc Pollefeys, Andreas Geiger, Tat-Jen Cham, and Jianfei Cai. Mvsplat: Efficient 3d gaussian splatting from sparse multi-view images. In *European Conference on Computer Vision*, pages 370–386. Springer, 2024.
- [6] Yuanxing Duan, Fangyin Wei, Qiyu Dai, Yuhang He, Wenzheng Chen, and Baoquan Chen. 4d-rotor gaussian splatting: towards efficient novel view synthesis for dynamic scenes. In *ACM SIGGRAPH 2024 Conference Papers*, pages 1–11, 2024.
- [7] Guangchi Fang and Bing Wang. Mini-splatting: Representing scenes with a constrained number of gaussians. In *European Conference on Computer Vision*, pages 165–181. Springer, 2024.
- [8] Yasutaka Furukawa and Jean Ponce. Accurate, dense, and robust multiview stereopsis. *IEEE Transactions on Pattern Analysis and Machine Intelligence*, 32(8):1362–1376, 2010.
- [9] Yuanyuan Gao, Hao Li, Jiaqi Chen, Zhengyu Zou, Zhihang Zhong, Dingwen Zhang, Xiao Sun, and Junwei Han. Citygs-x: A scalable architecture for efficient and geometrically accurate large-scale scene reconstruction. *arXiv preprint arXiv:2503.23044*, 2025.
- [10] Sharath Girish, Kamal Gupta, and Abhinav Shrivastava. Eagles: Efficient accelerated 3d gaussians with lightweight encodings. In *European Conference on Computer Vision*, pages 54–71. Springer, 2024.
- [11] Xiaodong Gu, Zhiwen Fan, Siyu Zhu, Zuozhuo Dai, Feitong Tan, and Ping Tan. Cascade cost volume for high-resolution multi-view stereo and stereo matching. In *Proceedings of the IEEE/CVF conference on computer vision and pattern recognition*, pages 2495–2504, 2020.
- [12] Antoine Guédon and Vincent Lepetit. Sugar: Surface-aligned gaussian splatting for efficient 3d mesh reconstruction and high-quality mesh rendering. In *Proceedings of the IEEE/CVF Conference on Computer Vision and Pattern Recognition*, pages 5354–5363, 2024.
- [13] Binbin Huang, Zehao Yu, Anpei Chen, Andreas Geiger, and Shenghua Gao. 2d gaussian splatting for geometrically accurate radiance fields. In *ACM SIGGRAPH 2024 conference papers*, pages 1–11, 2024.
- [14] Kaiwen Jiang, Venkataram Sivaram, Cheng Peng, and Ravi Ramamoorthi. Geometry field splatting with gaussian surfels. In *Proceedings of the Computer Vision and Pattern Recognition Conference*, pages 5752–5762, 2025.

- [15] Michael Kazhdan, Matthew Bolitho, and Hugues Hoppe. Poisson surface reconstruction. In *Proceedings of the fourth Eurographics symposium on Geometry processing*, volume 7, 2006.
- [16] Bernhard Kerbl, Georgios Kopanas, Thomas Leimkühler, and George Drettakis. 3d gaussian splatting for real-time radiance field rendering. *ACM Trans. Graph.*, 42(4):139–1, 2023.
- [17] Bernhard Kerbl, Andreas Meuleman, Georgios Kopanas, Michael Wimmer, Alexandre Lanvin, and George Drettakis. A hierarchical 3d gaussian representation for real-time rendering of very large datasets. *ACM Transactions on Graphics (TOG)*, 43(4):1–15, 2024.
- [18] Mingwei Li, Pu Pang, Hehe Fan, Hua Huang, and Yi Yang. TsGs: Improving gaussian splatting for transparent surface reconstruction via normal and de-lighting priors. In *Proceedings of the 33rd ACM International Conference on Multimedia*, pages 7220–7229, 2025.
- [19] Shujuan Li, Yu-Shen Liu, and Zhizhong Han. Gaussianudf: Inferring unsigned distance functions through 3d gaussian splatting. In *Proceedings of the Computer Vision and Pattern Recognition Conference*, pages 27113–27123, 2025.
- [20] Zhaoshuo Li, Thomas Müller, Alex Evans, Russell H Taylor, Mathias Unberath, Ming-Yu Liu, and Chen-Hsuan Lin. Neuralangelo: High-fidelity neural surface reconstruction. In *Proceedings of the IEEE/CVF Conference on Computer Vision and Pattern Recognition*, pages 8456–8465, 2023.
- [21] Zhihao Liang, Qi Zhang, Ying Feng, Ying Shan, and Kui Jia. Gs-ir: 3d gaussian splatting for inverse rendering. In *Proceedings of the IEEE/CVF Conference on Computer Vision and Pattern Recognition*, pages 21644–21653, 2024.
- [22] Jonathon Luiten, Georgios Kopanas, Bastian Leibe, and Deva Ramanan. Dynamic 3d gaussians: Tracking by persistent dynamic view synthesis. In *2024 International Conference on 3D Vision (3DV)*, pages 800–809. IEEE, 2024.
- [23] Ben Mildenhall, Pratul P Srinivasan, Matthew Tancik, Jonathan T Barron, Ravi Ramamoorthi, and Ren Ng. Nerf: Representing scenes as neural radiance fields for view synthesis. *Communications of the ACM*, 65(1):99–106, 2021.
- [24] Henrique Morimitsu, Xiaobin Zhu, Roberto M Cesar, Xiangyang Ji, and Xu-Cheng Yin. Dpflow: Adaptive optical flow estimation with a dual-pyramid framework. In *Proceedings of the Computer Vision and Pattern Recognition Conference*, pages 17810–17820, 2025.
- [25] Thomas Müller, Alex Evans, Christoph Schied, and Alexander Keller. Instant neural graphics primitives with a multiresolution hash encoding. *ACM transactions on graphics (TOG)*, 41(4):1–15, 2022.
- [26] Richard A Newcombe, Shahram Izadi, Otmar Hilliges, David Molyneaux, David Kim, Andrew J Davison, Pushmeet Kohi, Jamie Shotton, Steve Hodges, and Andrew Fitzgibbon. Kinectfusion: Real-time dense surface mapping and tracking. In *2011 10th IEEE international symposium on mixed and augmented reality*, pages 127–136. Ieee, 2011.
- [27] René Ranftl, Katrin Lasinger, David Hafner, Konrad Schindler, and Vladlen Koltun. Towards robust monocular depth estimation: Mixing datasets for zero-shot cross-dataset transfer. *IEEE transactions on pattern analysis and machine intelligence*, 44(3):1623–1637, 2020.
- [28] S.M. Seitz, B. Curless, J. Diebel, D. Scharstein, and R. Szeliski. A comparison and evaluation of multi-view stereo reconstruction algorithms. In *2006 IEEE Computer Society Conference on Computer Vision and Pattern Recognition (CVPR'06)*, volume 1, pages 519–528, 2006.
- [29] Mai Su, Zhongtao Wang, Huishan Au, Yilong Li, Xizhe Cao, Chengwei Pan, Yisong Chen, and Guoping Wang. Hug: Hierarchical urban gaussian splatting with block-based reconstruction for large-scale aerial scenes. In *Proceedings of the IEEE/CVF International Conference on Computer Vision*, pages 28839–28848, 2025.
- [30] Matias Turkulainen, Xuqian Ren, Iaroslav Melekhov, Otto Seiskari, Esa Rahtu, and Juho Kannala. Dn-splatter: Depth and normal priors for gaussian splatting and meshing. In *2025 IEEE/CVF Winter Conference on Applications of Computer Vision (WACV)*, pages 2421–2431. IEEE, 2025.
- [31] Peng Wang, Lingjie Liu, Yuan Liu, Christian Theobalt, Taku Komura, and Wenping Wang. Neus: Learning neural implicit surfaces by volume rendering for multi-view reconstruction. *arXiv preprint arXiv:2106.10689*, 2021.
- [32] Yuru Xiao, Deming Zhai, Wenbo Zhao, Kui Jiang, Junjun Jiang, and Xianming Liu. Mcgs: Multiview consistency enhancement for sparse-view 3d gaussian radiance fields. *IEEE Transactions on Pattern Analysis and Machine Intelligence*, 2025.
- [33] Gangwei Xu, Haotong Lin, Hongcheng Luo, Xianqi Wang, Jingfeng Yao, Lianghui Zhu, Yuechuan Pu, Cheng Chi, Haiyang Sun, Bing Wang, et al. Pixel-perfect depth with semantics-prompted diffusion transformers. *arXiv preprint arXiv:2510.07316*, 2025.
- [34] Lihe Yang, Bingyi Kang, Zilong Huang, Zhen Zhao, Xiaogang Xu, Jiashi Feng, and Hengshuang Zhao. Depth anything v2. *Advances in Neural Information Processing Systems*, 37:21875–21911, 2024.

- [35] Yixin Yang, Yang Zhou, and Hui Huang. Introducing unbiased depth into 2d gaussian splatting for high-accuracy surface reconstruction. In *Computer Graphics Forum*, volume 44, page e70252. Wiley Online Library, 2025.
- [36] Lior Yariv, Jiatao Gu, Yoni Kasten, and Yaron Lipman. Volume rendering of neural implicit surfaces. *Advances in neural information processing systems*, 34:4805–4815, 2021.
- [37] Mulin Yu, Tao Lu, Linning Xu, Lihan Jiang, Yuanbo Xiangli, and Bo Dai. Gsdf: 3dgs meets sdf for improved neural rendering and reconstruction. *Advances in Neural Information Processing Systems*, 37:129507–129530, 2024.
- [38] Zehao Yu, Anpei Chen, Binbin Huang, Torsten Sattler, and Andreas Geiger. Mip-splatting: Alias-free 3d gaussian splatting. In *Proceedings of the IEEE/CVF conference on computer vision and pattern recognition*, pages 19447–19456, 2024.
- [39] Zehao Yu, Torsten Sattler, and Andreas Geiger. Gaussian opacity fields: Efficient adaptive surface reconstruction in unbounded scenes. *ACM Transactions on Graphics (ToG)*, 43(6):1–13, 2024.
- [40] Chuanrui Zhang, Yingshuang Zou, Zhuoling Li, Minmin Yi, and Haoqian Wang. Transplat: Generalizable 3d gaussian splatting from sparse multi-view images with transformers. In *Proceedings of the AAAI Conference on Artificial Intelligence*, volume 39, pages 9869–9877, 2025.
- [41] Ziyu Zhang, Binbin Huang, Hanqing Jiang, Liyang Zhou, Xiaojun Xiang, and Shuhan Shen. Quadratic gaussian splatting: High quality surface reconstruction with second-order geometric primitives. In *Proceedings of the IEEE/CVF International Conference on Computer Vision*, pages 28260–28270, 2025.